Journal of Computational Physics **154,** 468–496 (1999)
Article ID jcph.1999.6323, available online at http://www.idealibrary.com on IDEAL®

Modeling Melt Convection in Phase-Field Simulations of Solidification

C. Beckermann,* H.-J. Diepers,† I. Steinbach,† A. Karma,‡ and X. Tong*

*Department of Mechanical Engineering, University of Iowa, Iowa City, Iowa 52242-1527;
†ACCESS e.V., Intzestraße 5, 52072 Aachen, Germany; ‡Department of Physics,
Northeastern University, Boston, Massachusetts 02115
E-mail: becker@icaen.uiowa.edu

Received November 24, 1998; revised April 22, 1999

A novel diffuse interface model is presented for the direct numerical simulation of microstructure evolution in solidification processes involving convection in the liquid phase. The solidification front is treated as a moving interface in the diffuse approximation as known from phase-field theories. The no-slip condition between the melt and the solid is realized via a drag resistivity in the diffuse interface region. The model is shown to accurately reproduce the usual sharp interface conditions in the limit of a thin diffuse interface region. A first test of the model is provided for flow through regular arrays of cylinders with a stationary interface. Then, two examples are presented that involve solid/liquid phase-change: (i) coarsening of a mush of a binary alloy, where both the interface curvature and the flow permeability evolve with time, and (ii) dendritic growth in the presence of melt convection with particular emphasis on the operating point of the tip.

Key Words: phase-field method; convection; dendritic growth; coarsening.

1. INTRODUCTION

The formation of morphological features in solidification of pure materials and alloys has been investigated over many years and the literature abounds in references on subjects as diverse as stability of a planar solid/liquid interface [1], dendritic growth [2], and coarsening of a solid/liquid mixture [3, 4]. The selection of solidification patterns is controlled by the interplay of thermal, solutal, capillary, and kinetic length or time scales [5]. Comparably little is known about the influence of natural or forced convection on microstructure development. Melt convection adds new length and time scales to the problem and results in morphologies that are potentially much different from those generated by purely diffusive heat and solute transport. Moreover, not only does convection influence the solidification pattern, but the evolving microstructure can also trigger unexpected and complicated flow phenomena.

0021-9991/99 $30.00

Examples are the coupled convective and morphological instabilities at a growth front investigated in detail by Coriell *et al*. [6] and Davis [7]. Other theoretical investigations involving convective effects are often of a preliminary nature, decoupling the flow from the interface evolution or applying only to limited parametric regions [8, 9]. The objective of the present study is to develop a numerical method that can be used to study nonlinear and fully coupled solidification and convection problems on a microscopic scale (first presented in [10]). The emphasis in this paper is not on describing intricate numerical procedures, but on deriving governing equations that can be easily implemented in standard codes for coupled transport phenomena.

The phase-field method has recently emerged as a viable computational tool for simulating the formation of complex interfacial patterns in solidification [11–13]. An overview of the origins of this method in the context of continuum models of phase transitions can be found in Karma and Rappel [14]. Udaykumar and Shyy [15] and Juric and Tryggvason [16] provide a detailed discussion of the relative merits of this method and other numerical techniques developed for solving problems with free interfaces that have a complex topology. The phase-field method belongs to a larger class of methods that rely on treating a microscopically sharp interface as a diffuse region immersed in the calculation domain. A variable ϕ, called the phase-field variable in the context of the phase-field method, is introduced that varies smoothly from zero to unity between the two phases over the diffuse interface region, which has a small but numerically resolvable thickness. This variable also serves to distribute the interfacial forces and other sources over the diffuse region.

The phase-field method derives its attractiveness from the fact that explicit tracking of the interface and explicitly satisfying interfacial boundary conditions is completely avoided. Other diffuse interface methods, such as the level set method [17], still require the accurate computation of interface normals and curvatures. This is accomplished in the phase-field method by solving a certain evolution equation for the phase-field variable. This evolution equation can be rigorously derived from thermodynamically consistent theories of continuum phase transitions (see, for example, Ref. [18]). In order to establish a clearer connection with other diffuse interface methods, we present in this paper a simpler though less general derivation starting from the classical velocity-dependent Gibbs–Thomson interface condition, which includes the effect of surface tension and the attachment kinetics of atoms at the interface. A key feature of the phase-field evolution equation is that it contains an explicit anti-diffusivity that maintains thin and well-defined interface regions without introducing oscillations or violating conservation of mass [19].

The phase-field method, as well as other techniques that rely on a diffuse interface, can be shown to reduce to the standard sharp-interface formulation in the limit of vanishing interface thickness [1]. In actual computations, it is critical to understand how the quality of the solution deteriorates with increasing interface thickness, because the grid spacing needs to be of the order of or smaller than the interface thickness. In the context of phase-field methods applied to solidification, Wheeler *et al*. [12] and Wang *et al*. [18] have shown that the interface thickness must be smaller than the capillary length for the solution to converge to the sharp-interface limit. Karma and Rappel [14] reexamined this issue and derived coefficients for the so-called thin-interface limit of the phase-field equation, where the interface thickness only needs to be small compared to the "mesoscale" of the heat and/or solute diffusion field, and the classical interface conditions are satisfied for a finite thickness. Their analysis allowed for the first time fully resolved computations to be made for three-dimensional dendrites with arbitrary interface kinetics [20]. In our derivation of

the model equations for the case of melt convection, we also use a thin-interface approach and show that the interface thickness only needs to be small compared to the mesoscale of the flow field.

Application of the phase-field and other diffuse interface methods to solidification has been limited to problems where the transport of heat and/or solute is by diffusion only. Jacqmin [19] recently presented an application of the phase-field method to two-phase Navier–Stokes flows driven by surface tension at the interface between two fluids. In particular, a more complete version of the continuum surface tension method of Brackbill *et al*. [21] was shown to result from the phase-field model. In this and other immersed interface techniques for two-fluid flows, not only are the interfacial forces modeled as continuum forces distributed over the diffuse interface region, but other fluid properties, for example, the density and viscosity, are also smeared over the interface region by varying them smoothly from their values in one fluid to the ones in the other fluid. In the present application to solidification with melt convection, we assume the solid phase to be rigid and stationary and surface tension driven flows are not considered. We introduce a distributed dissipative interfacial drag term in the Navier–Stokes equation that provides a consistent and accurate way of modeling the usual no-slip condition at a microscopically sharp interface. Our method can be used with any diffuse interface technique, but we present its application only in the context of the phase-field method. It is important to note that the present method does not rely on specifying a variable viscosity across the diffuse interface region that tends to a large value in the rigid solid. While such an approach may be physically realistic for certain classes of materials, the variation would be difficult to specify for a rigid solid. In addition, our method addresses in a physically realistic way the transport of mass, momentum, heat, and solute by the ”residual” flow in the diffuse interface region by including phase-field variable dependent advection terms in the conservation equations.

The diffuse interface versions of the mass, momentum, species, and energy conservation equations are derived next, which is followed by a geometrical derivation of the evolution equation for the phase-field variable ϕ. The model is first applied to one-dimensional Couette and Poiseuille flows with a stationary diffuse interface, as well as to flow around a more complicated “microstructure” consisting of regular arrays of cylinders. These test cases allow for a comparison with analytical solutions and an examination of the accuracy of the solution for increasing thickness of the diffuse interface. Then, two examples involving solidification with melt convection are presented. The first example is concerned with adiabatic coarsening of an isothermal solid/liquid mixture of a binary alloy with melt flow, finite-rate diffusion of solute in the solid phase, and convection of solute in the liquid phase. Both, the effects of convection on coarsening and the profound influence of coarsening on the flow, are demonstrated. The second example deals with the effect of convection on dendritic growth of a pure substance in a supercooled melt. The effect of the flow on the dendrite tip speed and curvature is investigated in some detail.

2. CONSERVATION EQUATIONS FOR A DIFFUSE INTERFACE

The conservation equations for mass, momentum, energy, and species are derived by treating the microscopically sharp solid/liquid interface as a diffuse region where the solid and liquid phases coexist. The phase-field variable, ϕ, varies smoothly from zero in the bulk liquid to unity in the solid and can be viewed as a volume fraction solid. Conservation

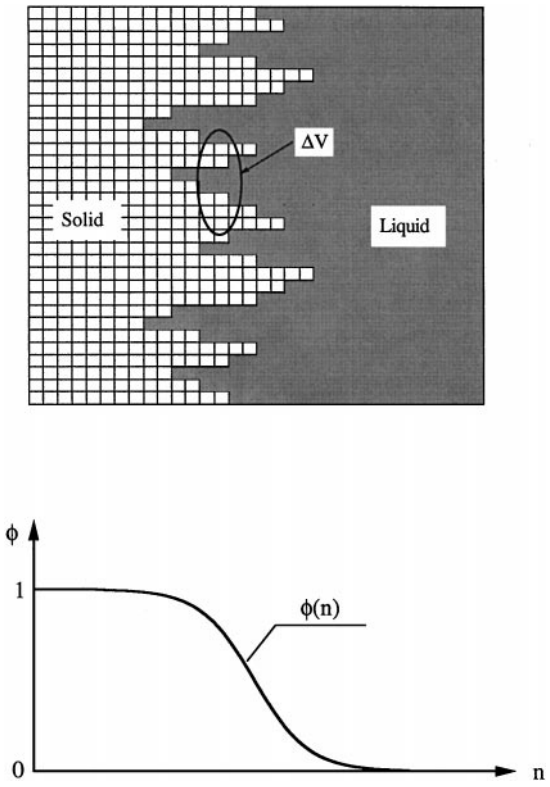

FIG. 1. Schematic illustration of the diffuse solid–liquid interface, the averaging volume, and the phase-field variable variation normal to the interface.

equations are needed that are valid not only in the solid and liquid phases, but also in the diffuse interface region. Our basic strategy in deriving such equations is to use the same kind of volume or ensemble averaging methods that have been used to derive conservation equations for other multiphase systems [22–24]. In solid/liquid phase change with a microscopically sharp interface, a diffuse interface region physically exists only on an atomic scale and can be associated with a density profile [25]. As shown in Fig. 1, the atomic-scale solid fraction is therefore defined for a representative elementary volume V_0, that is larger than the length scale associated with the atomic structures and much smaller than the diffuse interface region. It should not be confused with the solid fraction used in descriptions of mushy zones existing on a macroscopic [O(10^{-1} m)] scale.

The present approach results in physically meaningful model equations that are consistent not only with the phase-field but any diffuse interface method. Volume or ensemble averaging allows for a rigorous derivation of the conservation equations for multi-phase mixtures (i.e., for the diffuse interface) from the basic continuum equations for single-phase substances. One result of the averaging is that the surface forces and other sources at microscopically sharp interfaces are represented as volume forces and sources that are distributed over the diffuse interface region. Furthermore, the averaged conservation equations explicitly contain the phase-field variable and reduce to the correct forms in the limit of a sharp interface. The phase-field variable ϕ is formally related to the volume or ensemble average of an existence function, X_s , which is unity in the solid and zero otherwise [23],

via

$$\phi = \phi_s = 1 - \phi_l = \frac{1}{\Delta V} \int_{\Delta V} X_s \, dV = \langle X_s \rangle, \tag{1}$$

where the symbols $\langle\ \rangle$ denote an average over the volume ΔV, which is macroscopically small. The average interfacial area, ΔA_i, between the solid and liquid per unit volume is given by

$$\frac{\Delta A_i}{\Delta V} = \langle |\nabla X_s| \rangle = |\nabla \phi| \tag{2}$$

and the average unit normal vector exterior to the solid, $\mathbf{n}$, and curvature, κ, of the microscopic solid/liquid interface are defined by

$$\mathbf{n} = \left\langle -\frac{\nabla X_s}{|\nabla X_s|} \right\rangle = -\frac{\nabla \phi}{|\nabla \phi|} \tag{3}$$

and

$$\kappa = \nabla \cdot \mathbf{n} = -\frac{1}{|\nabla \phi|} \left[\nabla^2 \phi - \frac{(\nabla \phi \nabla)|\nabla \phi|}{|\nabla \phi|} \right]. \tag{4}$$

A general advection-diffusion equation, valid at a point within a phase k, for any conserved quantity Ψ can be expressed as

$$\frac{\partial}{\partial t}(\rho \Psi) + \nabla \cdot (\rho \mathbf{v} \Psi) + \nabla \cdot \mathbf{j} = 0, \tag{5}$$

where ρ, $\mathbf{v}$, and $\mathbf{j}$ are the density, velocity, and diffusive flux, respectively. Volumetric sources are not considered. Averaging this equation over ΔV yields the following general conservation equation for phase k in a multi-phase system [23]

$$\frac{\partial}{\partial t}\langle X_k \rho \Psi \rangle + \nabla \cdot \langle X_k \rho \mathbf{v} \Psi \rangle + \nabla \cdot \langle X_k \mathbf{j} \rangle - \left\langle [\rho \Psi (\mathbf{v} - \mathbf{v}_i) + \mathbf{j}]^k \cdot \nabla X_k \right\rangle = 0, \tag{6}$$

where $\mathbf{v}_i \cdot \nabla X_k = -\partial X_k / \partial t$ defines the velocity $\mathbf{v}_i$ of the interface. In the absence of interfacial sources (e.g., surface tension), the sum of the advective and diffusive fluxes across the interface, given by the last term in Eq. (6), must be equal on both sides of the interface.

In the following, we provide the averaged mass, momentum, energy, and species conservation equations for a simple binary alloy undergoing solid/liquid phase-change. Some of the details of the derivations can be found in Refs. [23, 24]. In order to keep the equations simple, the densities of the liquid and solid phases are assumed equal and constant, i.e., $\rho_s = \rho_l = \rho = \text{const}$. The intrinsic or phase average of a variable Ψ is defined by

$$\Psi_k = \langle X_k \Psi \rangle / \phi_k \tag{7}$$

and average mixture quantities by

$$\overline{\Psi} = \sum_{k=s,l} \langle X_k \Psi \rangle = \sum_{k=s,l} \phi_k \Psi_k. \tag{8}$$

The overbar is omitted in the following. Furthermore, all dispersive fluxes, arising from averages of the $\mathbf{v}\Psi$ product, and tortuosities in the diffusive fluxes are neglected as a first approximation. The solid is assumed to be stationary and rigid, i.e., $\mathbf{v}_s = 0$, such that a momentum equation for the solid phase is not needed.

Mass

The mixture continuity equation is obtained by summing the averaged solid and liquid continuity equations, which can be obtained by setting $\Psi = 1$ and $\mathbf{j} = 0$ in Eq. (6). Then,

$$\nabla \cdot [(1-\phi)\mathbf{v}_l] = 0, \tag{9}$$

where $\mathbf{v}_l$ is the averaged intrinsic liquid velocity and $(1-\phi) = \phi_l$.

Momentum

The averaged liquid ($k = l$) momentum equation can be derived from Eq. (6) by setting $\Psi = \mathbf{v}$ and $-\mathbf{j} = -P\mathbf{I} + \boldsymbol{\tau}$, where P is the pressure, $\mathbf{I}$ is the unit tensor (i.e., identity matrix $\delta_{i,j}$ in Cartesian coordinates), and $\boldsymbol{\tau}$ is the viscous stress tensor. Hence,

$$\begin{aligned}\frac{\partial}{\partial t}[(1-\phi)\rho\mathbf{v}_l] &+ \nabla \cdot [(1-\phi)\rho\mathbf{v}_l\mathbf{v}_l] \\ &= -\nabla[(1-\phi)P_l] + \nabla \cdot [(1-\phi)\boldsymbol{\tau}_l] + \left\langle [\rho\mathbf{v}(\mathbf{v}-\mathbf{v}_i) + P\mathbf{I} - \boldsymbol{\tau}]^l \cdot \nabla X_l \right\rangle. \end{aligned} \tag{10}$$

The interfacial momentum source term, i.e., the last term in Eq. (10), can be simplified by realizing that $[\mathbf{v}(\mathbf{v}-\mathbf{v}_i)]^l \cdot \nabla X_l = 0$ for equal densities of the phases and $\mathbf{v}_s = 0$. Furthermore, by defining an average interfacial pressure of the liquid, $P_{l,i}$, as [23]

$$P_{l,i}\nabla\phi_l = P_{l,i}\nabla(1-\phi) = \left\langle [P\mathbf{I}]^l \cdot \nabla X_l \right\rangle \tag{11}$$

and assuming that compressibility effects are negligible such that microscopic pressure equilibrium exists, i.e., $P_{l,i} = P_l$, the pressure contribution to the interfacial momentum source can be combined with the average pressure gradient term, i.e., the first term on the right-hand side of Eq. (10), to give $-(1-\phi)\nabla P_l$. Finally, the average viscous stress term, i.e., the second term on the right-hand side of Eq. (10), can be modeled for an incompressible Newtonian liquid with constant viscosity, μ_l, a stationary solid and equal phase densities, as [24]

$$\nabla \cdot [(1-\phi)\boldsymbol{\tau}_l] = \nabla \cdot (\mu_l \nabla[(1-\phi)\mathbf{v}_l]). \tag{12}$$

This model is in accordance with the usual theories of flow through porous media [22–24], where the average viscous stress is taken to be proportional to the gradient of the superficial liquid velocity, $(1-\phi)\mathbf{v}_l$. Now, Eq. (10) can be rewritten as

$$\begin{aligned}\frac{\partial}{\partial t}[(1-\phi)\rho\mathbf{v}_l] &+ \nabla \cdot [(1-\phi)\rho\mathbf{v}_l\mathbf{v}_l] \\ &= -(1-\phi)\nabla P_l + \nabla \cdot (\mu_l \nabla[(1-\phi)\mathbf{v}_l]) - \left\langle [\boldsymbol{\tau}]^l \cdot \nabla X_l \right\rangle. \end{aligned} \tag{13}$$

The last term on the right hand side of Eq. (10) accounts for the dissipative viscous stress in the liquid due to interactions with the solid in the diffuse interface region. This term is of key importance to the present study and is modeled in a subsequent section. Note that in the liquid ($\phi = 0$), Eq. (13) reduces to the usual single-phase Navier–Stokes equation for a Newtonian fluid with constant density and viscosity.

Energy

By summing up the averaged energy conservation equations for the solid and liquid phases and assuming that the heat flux is given by Fourier's law, we obtain the following mixture energy equation

$$\frac{\partial}{\partial t}(\rho h) + \nabla \cdot [(1-\phi)\rho \mathbf{v}_l h_l] = \nabla \cdot [\phi \lambda_s \nabla T_s + (1-\phi)\lambda_l \nabla T_l], \tag{14}$$

where h denotes the mixture enthalpy, $h = \phi h_s + (1-\phi)h_l$. Assuming equal and constant specific heats, i.e., $c_l = c_s = c_p$, and equal thermal conductivities, i.e., $\lambda_l = \lambda_s = \lambda$, defining the latent heat of fusion as $h_l - h_s = L$, and assuming locally equal phase temperatures, i.e., $T_l = T_s = T$, we obtain

$$\frac{\partial T}{\partial t} + \nabla \cdot [(1-\phi)\mathbf{v}_l T] = \alpha \nabla^2 T + \frac{L}{c_p}\frac{\partial \phi}{\partial t}, \tag{15}$$

where $\alpha = \lambda/(\rho c_p)$ is the thermal diffusivity.

Species

Again, summing up the averaged species equations for the solid and liquid phases and assuming that the diffusive species flux is given by Fick's law, the following mixture species equation is obtained [24, 26]

$$\frac{\partial}{\partial t}[\phi C_s + (1-\phi)C_l] + \nabla \cdot [(1-\phi)\mathbf{v}_l C_l] = \nabla \cdot [\phi D_s \nabla C_s + (1-\phi) D_l \nabla C_l], \tag{16}$$

where C_k and D_k are the species concentration and binary mass diffusivity, respectively, for each phase. Before Eq. (16) can be solved, a relationship between the species concentrations in the solid, C_s , and liquid, C_l , needs to be found. Assuming local equilibrium on the atomic scale (as with the temperatures), a binary partition coefficient can be defined as

$$k = \frac{C_s}{C_l}. \tag{17}$$

Defining an average mixture concentration, C, according to Eq. (8), the phase concentrations can be expressed as

$$C_s = \frac{kC}{1-\phi+k\phi} \qquad \text{and} \qquad C_l = \frac{C}{1-\phi+k\phi} \tag{18}$$

and Eq. (16) can be rewritten as

$$\frac{\partial C}{\partial t} + \nabla \cdot \left(\frac{1-\phi}{1-\phi+k\phi}\mathbf{v}_l C\right) = \nabla \cdot \tilde{D}\left[\nabla C + \frac{(1-k)C}{1-\phi+k\phi}\nabla \phi\right], \tag{19}$$

where

$$\tilde{D} = D_s + (D_l - D_s)\frac{1-\phi}{1-\phi+k\phi}. \tag{20}$$

Equation (19) can be solved for the mixture concentration. Then, the solid and liquid concentrations are obtained from Eq. (18). The present mixture species conservation equation has a clear physical interpretation. The prefactor before the velocity in Eq. (19) implies that only the liquid species are advected with the superficial liquid velocity, $(1-\phi)\mathbf{v}_l$. The effective diffusion coefficient, $\tilde{D}$, can be viewed as a mixture diffusivity. The last term in Eq. (19) is a diffusive flux that is proportional to the segregation amount $\frac{(1-k)C}{1-\phi+k\phi} = C_l - C_s$ and is in the direction of the average interface normal (i.e., across the interface).

It is interesting to make contact with existing models of alloy solidification [12, 27, 28], as well as the basic thermodynamics of dilute alloys, by noting that Eq. (19) can be rewritten (for simplicity without flow) in a variational form

$$\frac{\partial C}{\partial t} = \nabla \cdot \left(M \nabla \frac{\delta F}{\delta C} \right) \tag{21}$$

similar to the Cahn–Hillard equation [29]. In this context, $M = \tilde{D}C$, can be interpreted as an atomic mobility, and the function

$$F(\phi, C) = C \ln\left[\frac{C}{1-\phi+k\phi}\right] - C + \Phi(\phi, \nabla\phi, \ldots) \tag{22}$$

as the bulk free-energy of the system, where $\Phi(\phi, \nabla\phi, \ldots)$ is an arbitrary function of ϕ and its higher gradients that does not appear in Eq. (19) after taking the functional derivative in Eq. (21). Consequently, the chemical potential, $\mu = \partial F/\partial C = \ln[C/(1-\phi+k\phi)]$, equals $\ln C_l$ in the liquid phase ($\phi = 0$) and $\ln C_s$ in the solid phase ($\phi = 1$), which are precisely the standard entropic contributions derived from first principles of thermodynamics [30]. Therefore, it is interesting that although Eq. (19) is derived from an averaging method, as opposed to variationally, it can be given a proper thermodynamic interpretation. However, one difference between the present model and other phase-field models of alloy solidification [12, 27, 28] is that we shall not require the equations for ϕ and C to be derivable from a single free-energy functional. For example, we shall not require that the equation of motion for ϕ, described in the next section, be of the form $\dot{\phi} \sim -\delta F/\delta\phi$, where F is the free-energy defined by Eq. (22). Relaxing this gradient flow constraint on the equations generally provides more flexibility in the choice of the phase-field model, and even some computational advantages [20]. We stick here to the point of view that the phase-field equations are only quantitatively meaningful in the sharp-interface limit where they can be ultimately related to experiment.

3. PHASE-FIELD EQUATION

We present a simple geometrically motivated derivation of the phase-field equation starting from the phenomenological Gibbs–Thomson interface relation. The derivation is only intended to clarify the connection between the phase-field method and other immersed interface techniques that utilize a diffuse interface.

The Gibbs–Thomson equation for an isotropic surface energy and a simple binary alloy can be written as

$$\frac{v_n}{\mu_k} = T_m - T + m_l C_l - \Gamma\kappa, \tag{23}$$

where v_n is the normal interface speed, μ_k is a linear kinetic coefficient, T_m is the equilibrium melting temperature of the pure substance, m_l is the slope of the liquidus line from an equilibrium phase diagram, and Γ is the Gibbs–Thomson coefficient. The normal interface speed is given by

$$v_n = \mathbf{v}_i \cdot \mathbf{n} = \mathbf{v}_i \cdot \left(-\frac{\nabla\phi}{|\nabla\phi|}\right) = \frac{\partial\phi/\partial t}{|\nabla\phi|}. \tag{24}$$

Substituting Eq. (24) and the expression for the curvature, κ, given by Eq. (4), into Eq. (23) yields

$$\frac{\partial\phi}{\partial t} = v_n|\nabla\phi| = \mu_k\Gamma\left[\nabla^2\phi - \frac{(\nabla\phi\nabla)|\nabla\phi|}{|\nabla\phi|}\right] + \mu_k(T_m - T + m_l C_l)|\nabla\phi|. \tag{25}$$

Equation (25) does not have a unique solution for a stationary front profile for ϕ. Such a profile has to be specified separately and corresponds to the choice of a kernel. Unlike in other diffuse interface methods, the profile is physically motivated in the phase-field method. The most commonly used profile results from the choice of a double-well potential for the Gibbs free energy in the derivation of the phase-field equation [12, 13]. The profile is given by

$$\phi = \frac{1}{2}\left(1 - \tanh\frac{n}{2\delta}\right), \tag{26}$$

where n is the coordinate normal to the interface and 6δ is the interface thickness over which ϕ varies from 0.05 to 0.95. With Eq. (26), the average interfacial area per unit volume is given by

$$|\nabla\phi| = \frac{\partial\phi}{\partial n} = \frac{\phi(1-\phi)}{\delta} \tag{27}$$

and the second term in the expression for the curvature, Eq. (4), becomes

$$\frac{(\nabla\phi\nabla)|\nabla\phi|}{|\nabla\phi|} = \frac{\partial^2\phi}{\partial n^2} = \frac{\phi(1-\phi)(1-2\phi)}{\delta^2}. \tag{28}$$

Substituting Eqs. (27) and (28) into Eq. (25) results in the present phase-field-like equation

$$\frac{\partial\phi}{\partial t} = \mu_k\Gamma\left[\nabla^2\phi - \frac{\phi(1-\phi)(1-2\phi)}{\delta^2}\right] + \mu_k(T_m - T + m_l C_l)\frac{\phi(1-\phi)}{\delta} \tag{29}$$

which has for a stationary profile Eq. (26) in equilibrium, $T = T_m + m_l C_l$. The last term in Eq. (29) represents the thermo-solutal driving force for ϕ, while the first term on the right-hand side represents surface tension and is an anti-diffusivity that maintains a thin and well-defined interface.

In a non-stationary growth situation, the instantaneous profile of ϕ along the local normal direction will only differ slightly from the stationary profile defined by Eq. (26) if δ is small, such that in the limit $\delta \to 0$, the phase-field equation faithfully reproduces the interface condition Eq. (23). Using a reformulated asymptotic analysis of the phase-field model of a pure melt ($C_s = C_l = 0$), Karma and Rappel [20] have recently shown that there are corrections to this interface condition when δ is small compared to the macro scale of the diffusion field, but finite, which is the typical case in computations. If one applies the result of their analysis to the phase-field equation, Eq. (29), coupled to the transport equation, Eq. (15), and converts the result to the present notation, one obtains the standard interface condition, $v_n/\mu_k^{eff} = T_m - \Gamma_\kappa$, where

$$\frac{1}{\mu_k^{eff}} = \frac{1}{\mu_k}\left[1 - A\frac{\delta}{\alpha}\frac{\mu_k L}{c_p}\right] \qquad (C_l = 0). \tag{30}$$

μ_k^{eff} is an effective kinetic coefficient and $A = 5/6$. Note that the finite δ correction to the interface condition originates from the variation of the temperature field in the interface region. For this reason, both α and L/c_p appear in the expression for μ_k^{eff}. One nice feature of this result is that one can choose the dimensionless combination of parameters $A\delta\mu_k L/\alpha c_p = 1$ and reproduce the condition of local equilibrium at the interface (i.e., instantaneous attachment kinetics), which is experimentally relevant at low growth rate. It should be emphasized that Eq. (30) is only valid for pure melts. For the case of isothermal alloy solidification, i.e., Eq. (29) coupled to the transport Eq. (19) with uniform T, an analysis similar to that of Ref. [20] leads to the conclusion that the finite δ corrections to the interface condition do not simply lead to a renormalization of the kinetic coefficient [31]. There is generally a discontinuity of chemical potential at the interface and the corrections to the interface concentration on the two sides of the interface are proportional to the normal gradient of solute at the interface [31]. For the study of isothermal coarsening presented in Section 7, these corrections appear to have a small effect on the dynamics since we recover scaling laws that agree with sharp interface theories. This is consistent with the fact that these additional corrections to the interface condition (discontinuity of chemical potential and gradient corrections) are proportional to the interface velocity. This velocity is generally small during coarsening, except during the coalescence or disappearance of particles. In contrast, during dendritic growth, small kinetic variations of temperature along the interface can profoundly influence the selection of the operating state [32]. Therefore, in this case, it is important to include such corrections.

4. MODELING OF THE INTERFACIAL STRESS TERM

Central to the present method is the modeling of the dissipative interfacial stress term, $\mathbf{M}_l^d$, in the momentum equation for the liquid, Eq. (13), i.e., $\langle [\boldsymbol{\tau}]^l \cdot \nabla X_l \rangle$. Noting the delta-function like properties of the ∇X_k operator, this term can be rewritten as

$$\mathbf{M}_l^d = \left\langle [\boldsymbol{\tau}]^l \cdot \nabla X_l \right\rangle = \boldsymbol{\tau}_{l,i} \cdot \nabla \phi_l = -\boldsymbol{\tau}_{l,i} \cdot \nabla \phi = \boldsymbol{\tau}_{l,i} \cdot \mathbf{n} |\nabla \phi|, \tag{31}$$

where $\boldsymbol{\tau}_{l,i}$ is the average viscous stress tensor at the interface. The viscous stress is generally proportional to the liquid viscosity and a velocity gradient. As a first approximation, and in

analogy with the friction term used for slow flow in porous media [24], we can write

$$\mathbf{M}_l^d = h\mu_l\phi\frac{\mathbf{v}_l}{\delta}|\nabla\phi|, \tag{32}$$

where h is a dimensionless constant. In Eq. (32), we have assumed that $\mathbf{v}_l$ varies linearly across the diffuse interface of thickness δ. The inclusion of the phase-field variable, ϕ, is strictly not necessary, but corresponds physically to an increasing interfacial stress with "solid fraction." The constant h is similar to a dimensionless friction coefficient and its value is determined analytically in the next section. Substituting Eq. (27) for the interfacial area per unit volume, $|\nabla\phi|$, the final expression suitable for computations is obtained as

$$\mathbf{M}_l^d = \mu_l\frac{h\phi^2(1-\phi)}{\delta^2}\mathbf{v}_l. \tag{33}$$

The drag term vanishes in the single-phase liquid ($\phi = 0$). In the limit of a sharp interface, $\delta \to 0$, the prefactor in Eq. (33) becomes infinitely large, thus reproducing the usual no-slip condition ($\mathbf{v}_l = 0$) at the solid/liquid interface. For a diffuse interface region of small but finite thickness, as is the case here, the above friction term acts as a distributed momentum sink that gradually forces the liquid velocity to zero as $\phi \to 1$.

5. ASYMPTOTICS FOR PLANE FLOW PAST A STATIONARY SOLID–LIQUID INTERFACE

The properties of the present model for the dissipative interfacial stress can be examined in detail for a simple flow which can be described analytically. Such a basic flow is plane Poiseuille flow past a stationary solid–liquid interface. By performing an asymptotic analysis, matching the inner solution in the diffuse interface region with the correct outer velocity profile corresponding to a sharp interface (i.e., with a no-slip condition at $\phi = 0.5$), the dimensionless constant h in Eq. (33) is determined.

Consider Poiseuille flow between two parallel plates oriented along the y-axis and with the plates located at $x = 0$ and $x = 2L$ (Fig. 2). The solid–liquid interface is assumed to be stationary and is represented by the lower plate (at $x = 0$). In the case of a sharp interface, the momentum equation is

$$\mu_l\frac{d^2v_l}{dx^2} = \frac{dP}{dy} = -\mu_l F, \tag{34}$$

where v_l is the y-component of the liquid velocity, dP/dy is the applied pressure gradient, and F is a short-hand notation for the pressure drop per unit length and viscosity. The solution of Eq. (34), applying no-slip conditions at the plates, is

$$v_l = xFL[1 - x/(2L)]. \tag{35}$$

For the diffuse interface case, the corresponding momentum equation is obtained from Eq. (10) as

$$\mu_l\frac{d^2(1-\phi)v_l}{dx^2} - h\mu_l\frac{\phi^2(1-\phi)}{\delta^2}v_l = (1-\phi)\frac{dP}{dy}. \tag{36}$$

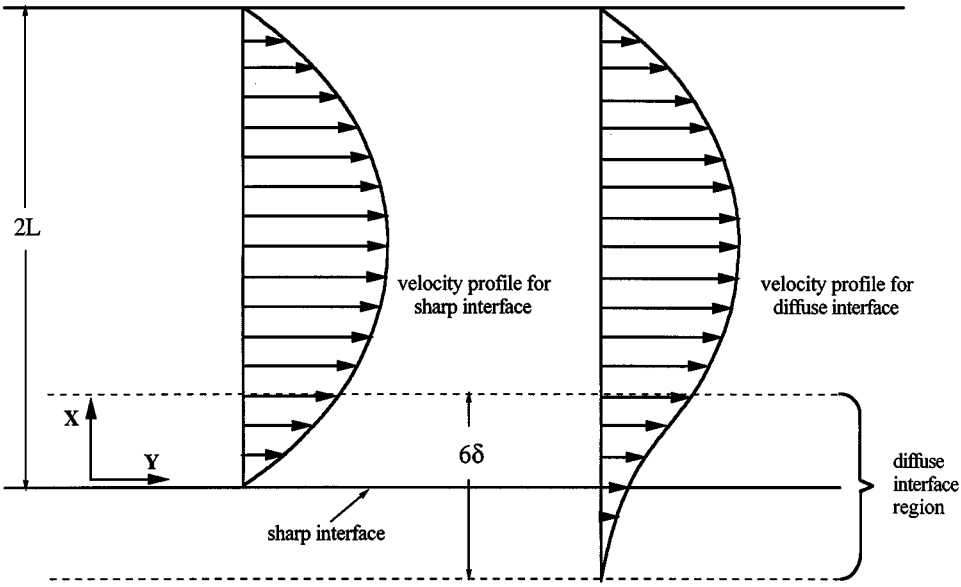

FIG. 2. Schematic illustration of the velocity profiles for Poiseuille flow with a sharp and a diffuse interface representing the lower boundary.

Introducing the inner variable $X = x/\delta$ and the mixture velocity $v = (1-\phi)v_l$, and using the same definition of F as above, yields

$$\frac{d^2v}{dX^2} - h\phi^2 v = -\delta^2 F(1-\phi). \tag{37}$$

We will first consider the limit of small δ, where the right-hand side of Eq. (37) can be neglected such that

$$\frac{d^2v}{dX^2} - h\phi^2 v = 0. \tag{38}$$

This limit corresponds to a linear velocity profile in the region outside the diffuse interface (Couette flow). We now seek to match the inner solution of Eq. (38) to the outer solution defined by Eq. (35) in the liquid, and zero velocity in the solid. Therefore, the matching conditions are

$$v(X \to -\infty) = 0 \tag{39}$$

and

$$v = (FL\delta)X \qquad \text{for } 1 \ll X \ll L/\delta. \tag{40}$$

Let us now consider the analytic asymptotic behavior of $v(X)$ for $|X| \gg 1$. For a general value of h we have

$$v(X) = A\exp(\sqrt{h}X) \qquad \text{for } X < 0 \tag{41}$$

$$v(X) = A\alpha(h)[X - X_i(h)] \qquad \text{for } X > 0, \tag{42}$$

where A is a constant and $\alpha(h)$ and $X_i(h)$ are functions of h only. Since Eq. (42) is linear, A can be chosen such that

$$A = FL\delta/\alpha(h). \tag{43}$$

However, $X_i(h)$, which is the effective interface position where the flow velocity vanishes, is only zero for a special value of $h = h^\star$ that needs to be determined. Hence, the matching condition given by Eq. (40) can only be satisfied if $X_i(h^\star) = 0$. By solving Eq. (35) with a fourth-order Runge–Kutta ODE solver, the value of $h^\star$ was determined to be

$$h^\star = 2.757. \tag{44}$$

The important property of $h^\star$ is that it does not depend on the imposed pressure gradient and flow field in the outer region. The present result holds for more general flows because in the limit of small δ there is always a linear velocity gradient normal to the interface. In addition, an extension of the analysis of Karma and Rappel [20] to the present model leads to the result that the tangential flow inside the thin interface region does not modify the velocity-dependent Gibbs–Thomson condition, $v_n/\mu_k^{eff} = T_m - T - \Gamma\kappa$, and the expression for the effective kinetic coefficient Eq. (30), which remains applicable with flow.

For the case of a linear velocity profile (Couette flow), the behavior of the solution for different values of h and different interface thicknesses δ is shown in Fig. 3. It can be seen that for $h \gg 2.757$, the velocity profile for the diffuse interface does not match the "exact" linear profile for a sharp interface but is significantly shifted. On the other hand, for $h = 2.757$, there is a perfect match regardless of the diffuse interface thickness. This independence of h on the interface thickness is the main advantage of the present method.

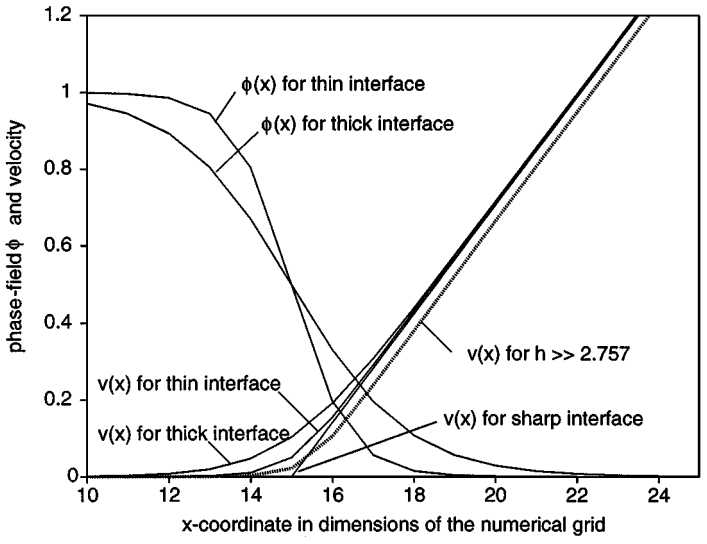

FIG. 3. Computed velocity profiles for Couette flow past a stationary solid–liquid interface; results are shown for two different interface thicknesses and the dimensionless interface friction coefficient $h = 2.757$, as well as for a thin interface with $h \gg 2.757$.

While the independence of $h^\star$ on the interface thickness δ is true for an infinite liquid region (i.e., $\delta/L \to 0$), it is useful to examine how $h^\star$ changes with finite δ/L. Let us define the small parameter

$$\varepsilon = \delta/L \tag{45}$$

and a dimensionless velocity

$$\tilde{v} = \frac{v}{FL\delta}. \tag{46}$$

Then, Eq. (37) becomes

$$\frac{d^2\tilde{v}}{dX^2} - h\phi\tilde{v} = -\varepsilon(1-\phi). \tag{47}$$

We are now looking for a solution of the above equation for small ε that matches the exact Poiseuille flow

$$\tilde{v} = X(1 - \varepsilon X/2) \qquad \text{for } |X \gg 1| \tag{48}$$

and decays to zero in the solid

$$\tilde{v}(X \to -\infty) = 0. \tag{49}$$

There is again a unique value of $h = h^\star(\varepsilon)$ for which this is possible, but which now depends on ε. A plot of $h^\star(\varepsilon)$ is shown in Fig. 4. For ε increasing to 0.1, $h^\star$ decreases by only about 5%. Such small changes in $h^\star$ have a negligible effect on the computed velocity profile outside the diffuse interface region. Figure 5 shows computed velocity profiles for different $\varepsilon = \delta/L$ for Poiseuille flow. Already for $\phi < 0.2$, and certainly in the pure liquid region, the diffuse interface profiles match the exact profile for a sharp interface at $\phi = 0.5$ extremely

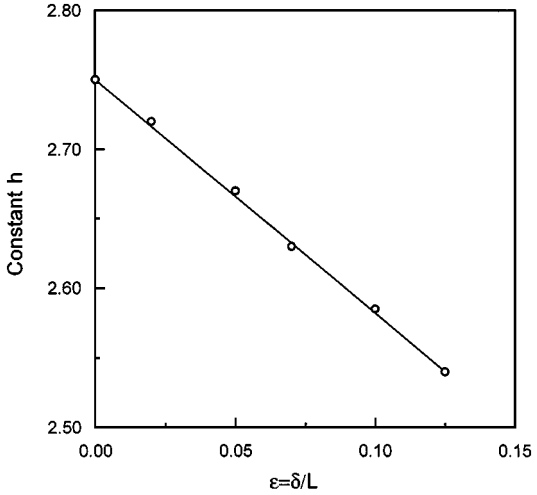

FIG. 4. Dependence of the dimensionless interface friction coefficient h on the ratio of the interface thickness to the half-width of the flow passage, ε, in Poiseuille flow.

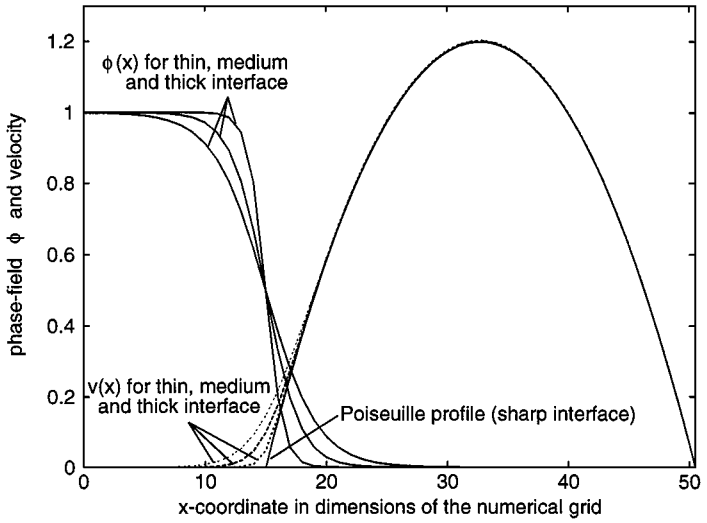

FIG. 5. Computed velocity profiles for Poiseuille flow in a channel where the lower boundary is a stationary solid–liquid interface (see Fig. 2); results are shown for three different interface thicknesses.

well. For a general flow, one should use the constant $h^{\star}(\varepsilon = 0)$ and decrease ε until the dependence on ε becomes negligible.

6. VALIDATION FOR TWO-DIMENSIONAL FLOW

A stringent test problem for the performance of the present diffuse interface model is given by Stokes flow through regular arrays of infinite cylinders as shown in Fig. 6. Unit cells containing both square and triangular arrangements are considered. The flow is periodic in the horizontal direction, forced by an external pressure gradient, and symmetric at the top and bottom boundaries. Analytical expressions for the drag force on the cylinders as a function of the solid fraction, f_s, in the unit cell have been obtained by Sangani and Acrivos [33] and Drummond and Tahir [34]. This test problem thus allows for a close examination of the ability of the present method to give the correct forces on a body, in particular for flow past a curved interface. In addition, the results for larger solid fractions, when the cylinders almost touch each other, provide a test for cases where the ratio of the interface thickness to the width of the flow passage (i.e., ε) is not small.

The two-dimensional momentum and continuity equations were solved numerically using a standard control-volume, implicit discretization scheme [35]. The distribution of the phase-field variable ϕ was set before a computational run using a radially symmetric tangent hyperbolic profile to affect the smearing of the (stationary) solid/liquid interface. This is illustrated by the variation of gray tones in Fig. 6. A square grid of 51×51 control-volumes was utilized in the simulations for the square array, and 52×45 for the triangular array. The interface thickness corresponded to about five control-volumes. The numerical results, together with the analytical predictions, are plotted in Figs. 7a and 7b. The mean liquid velocity through the unit cell is normalized by the pressure drop per unit width (drag force) and $4\pi\mu_l$. It can be seen that the numerical results are generally in excellent agreement with the exact Stokes flow solutions. Minor deviations are present for small solid fractions, which can be attributed to the relatively coarse numerical grid used. For the

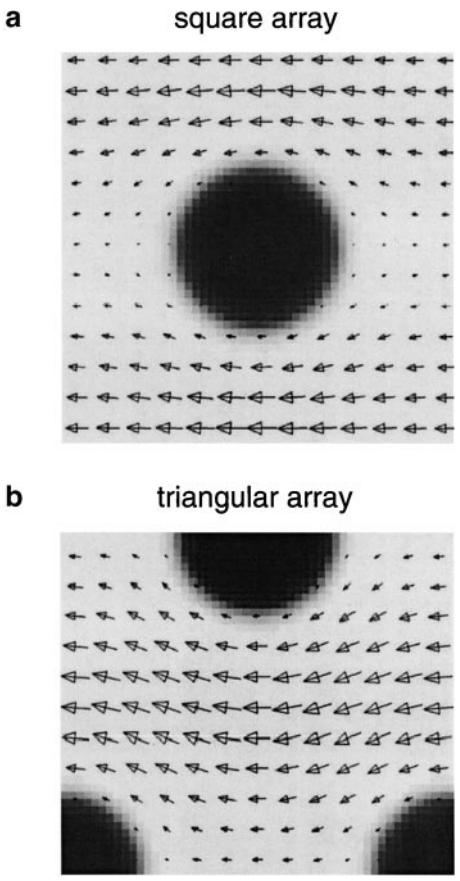

FIG. 6. Unit-cells and sample computed velocities for the simulation of flow through regular arrays of infinite cylinders; the flow is periodic in the east–west direction and the diffuse solid–liquid interface is reflected by the gray levels: (a) square array; (b) triangular array.

smallest volume fraction, the diameter of the cylinders (measured at $\phi = 0.5$) contains only six grid cells, implying that the diffuse interface thickness is of the same magnitude as the cylinder diameter. Nonetheless, remarkably accurate results are obtained. For the square array (Fig. 7a), large differences in the predictions occur for solid fractions greater than about 0.5. This can be attributed to the fact that the analytical solutions break down in this regime. The present numerical method correctly predicts the mean velocity approaching zero when the packing fraction is reached. No such disagreement exists for the triangular array (Fig. 7b). The computational results at high solid fractions, when the diffuse interfaces from neighboring cylinders almost overlap, show that the present model has excellent convergence properties for large interface thickness to flow passage width ratios (i.e., ε). Our preliminary tests indicate that other methods, including the popular smeared viscosity approach (see Introduction), are unlikely to produce results of similar accuracy for large ε.

7. EXAMPLE 1: SIMULATION OF CONVECTION AND COARSENING IN AN ISOTHERMAL MUSH OF A BINARY ALLOY

As a first application involving solid/liquid phase-change, the capillary-driven coarsening of and flow through a mush of an Al-4 wt.% Cu alloy is simulated. The two-dimensional

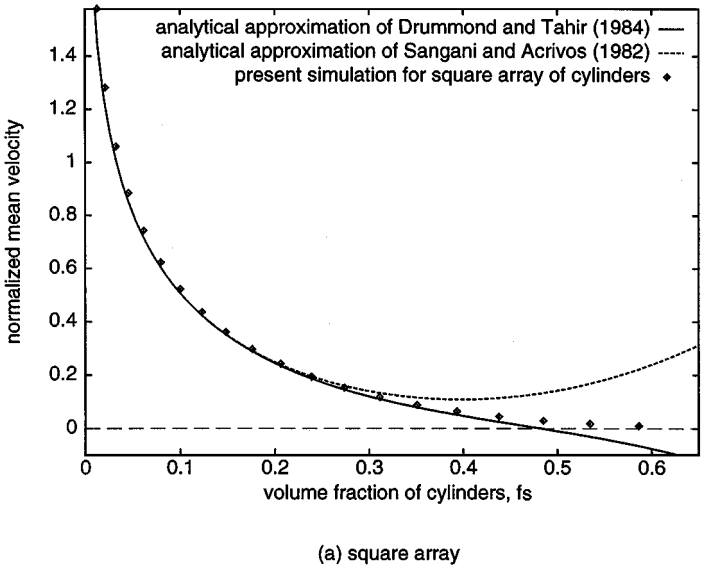

(a) square array

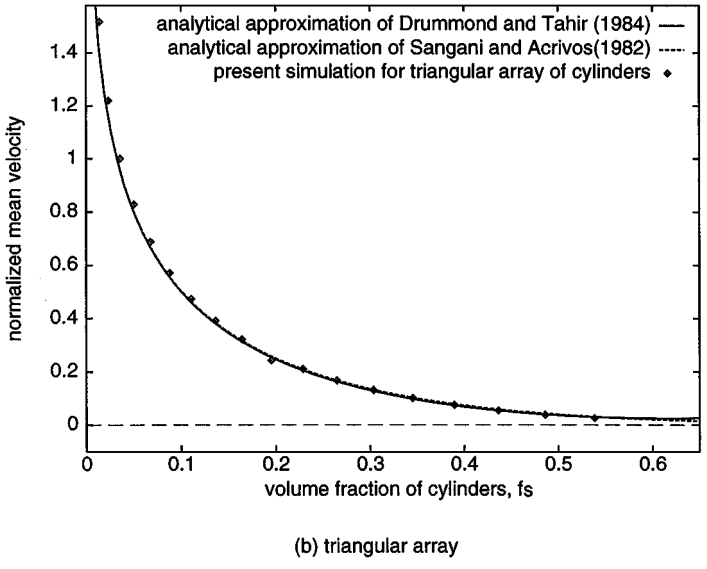

(b) triangular array

FIG. 7. Comparison of the computed normalized mean velocities through regular arrays of cylinders (see Fig. 6) as a function of the volume fraction of cylinders with the analytical results of Sangani and Acrivos [33] and Drummond and Tahir [34]: (a) square array; (b) triangular array.

system consists of a random array of cylinders, which can be interpreted as a cross section through an array of dendrites. The initial size distribution of the cylinders is set according to the coarsening theory of Marqusee [36]. Periodic and/or symmetric conditions are applied at the boundaries of the square domain of size 0.81 mm^2. The system is assumed to be isothermal, such that its temperature can be evaluated from the conservation law

$$\rho c_p T = L f_s. \tag{50}$$

TABLE I
Thermophysical Properties Used in the Al–4%Cu Coarsening Simulations [10]

Property	Value
T_m	933.6 K
m_l	2.6 K/%
Γ	2.41×10^{-7} mK
D_l	3×10^{-9} m^2/s
D_s	3×10^{-13} m^2/s
K	0.14
ρL	9.5×10^{8} J/m^3
ρc_P	2.58×10^{6} J/Km^3
ρ	2.475×10^{3} kg/m^3
μ	0.014 Poise
6δ	1.27×10^{-5} m
μ_k	2.6×10^{-5} m/sK

Note. For practical reasons the value of δ was chosen to be approximately equal to the length of one grid cell—the actual interface thickness, $6\delta^{act.}$, is of the order of 10^{-9} m; the actual kinetic coefficient, $\mu_k^{act.}$, is approximately 0.33 m/sK. The value in the table was obtained by multiplying $\mu_k^{act.}$ by the ratio $\delta^{act.}/\delta$.

The initial mean solid fraction, f_s, for all simulations reported here is 20.7%. The initial concentration distribution in each cylinder and the melt is set according to the Scheil equation. All material data are summarized in Table I. The simulations are performed on a 301×301 grid and for a sufficiently long time to achieve self-similar coarsening behavior. Computed results for a simulation case without convection are shown in Figs. 8a–8d. The gray tones indicate the copper concentration, while the thick solid lines show the position of the solid/liquid interface ($\phi = 0.5$). It can be seen that the different curvature supercoolings of the various size cylinders cause concentration gradients to develop in the liquid between the solid, through which the cylinders exchange species by diffusion. This causes the larger cylinders to grow at the expense of the smaller cylinders, leading to the expected coarsening behavior. High concentration gradients are notable during coalescence of two cylinders, because negative curvatures result in an enhanced interface concentration according to the Gibbs–Thomson relation. At later times, a complex concentration distribution develops in the solid, reflecting the time history of the melting and resolidification processes.

Figures 8e–8h show predictions for a case with the same initial conditions as in the previous case, but with a melt flow through the system from the top to the bottom. The flow is driven by a constant externally imposed pressure drop of 0.2 N/m^2. The flow advects solute in the liquid, leading to a markedly different coarsening behavior. This is illustrated in Fig. 9, which shows a comparison of the evolution of the total interfacial area per unit depth, S, between the diffusive and convective cases. In both cases, coarsening leads to a reduction in the interfacial area with time. In the diffusive case, the long-time behavior is described by a coarsening law of the form $S \sim t^{-1/3}$. The coarsening exponent of $-1/3$ is in perfect agreement with LSW theory [3, 4]. On the other hand, the coarsening exponent in the convective case is $-1/2$, indicating a faster coarsening rate. The exponent of $1/2$ is

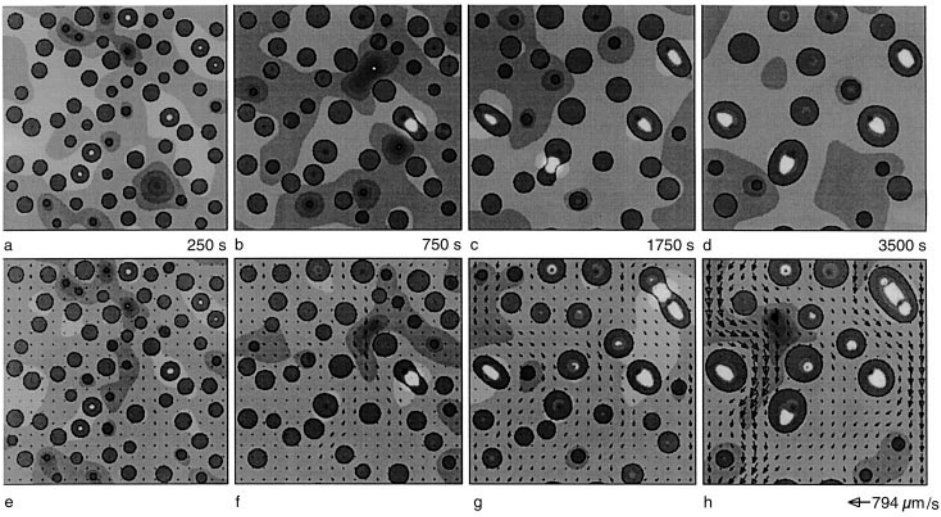

FIG. 8. Time histories for 2D coarsening simulations of an Al–4% Cu alloy mush with an initial solid fraction of 20.7% (approximately constant); the black contour lines correspond to $\Phi = 0.5$ and show the position of the solid–liquid interface; the gray shades indicate the Cu concentrations in the liquid (10 equal intervals between 4.861 and 4.871%) and solid (4 equal intervals between 0.682 and 0.6805%): (a) to (d) are purely diffusive conditions; (e) to (h) with forced convection in the north–south direction.

in agreement with the analysis of Ratke and Thieringer [37] for coarsening in the presence of a Stokes flow.

It can also be observed from Figs. 8e–8h that the flow velocities are continually increasing with time, although the imposed pressure drop is constant. The increase simply reflects the decrease in fluid friction due to a reduction in the interfacial area. For slow flow through a porous medium, the mean velocity, U, can be related to the pressure drop, ΔP, across the

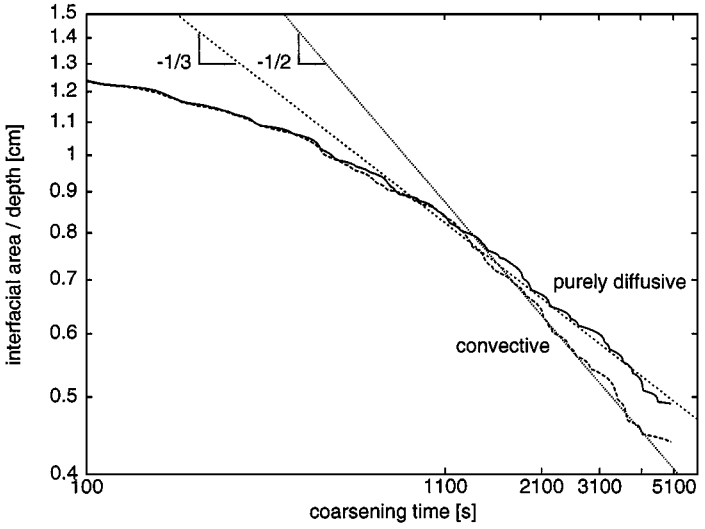

FIG. 9. Evolution of the total interfacial area per unit depth in the 2D coarsening simulations for purely diffusive conditions and with melt convection.

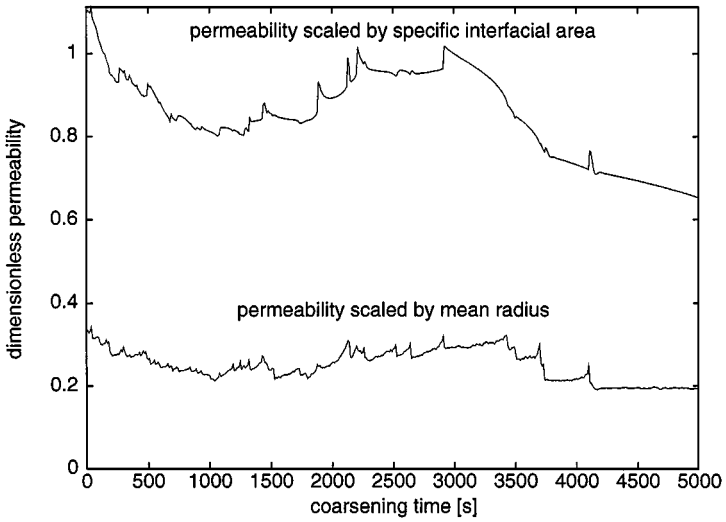

FIG. 10. Evolution of the permeability normalized either by the interfacial area per unit depth or the mean radius in the 2D coarsening simulations with melt convection.

system of length L by Darcy's law as

$$\mu_l U = K \Delta P / L, \tag{51}$$

where K is the permeability. Hence, the increase in the mean velocity implies an increase in the permeability. The above equation allows for the calculation of the permeability from the present simulation results. Figure 10 shows the variation of the permeability with time. The two curves correspond to the permeability normalized with the interfacial area ($K \cdot S^2$) and with the mean radius (K/R^2). Due to this normalization, the permeability is, as expected, approximately constant with time. The mean radius appears to provide slightly better scaling. The fluctuations in both curves are due to the limited number of cylinders used in the simulation, which leads to relatively abrupt changes in the mean flow when a cylinder disappears or when two cylinders coalesce. The fact that the radius normalized permeability is constant implies not only Stokes flow behavior (i.e., $U \sim R^2$), but also confirms the coarsening exponent of $1/2$.

Overall, the above simulations provide a good illustration of the capabilities of the present model. Although the results are shown to be realistic, a more detailed analysis and parametric studies are desirable to fully understand the system behavior. This will be presented in the near future.

8. EXAMPLE 2: DENDRITIC GROWTH IN THE PRESENCE OF CONVECTION

The second application of the present model involves equiaxed dendritic growth of a pure substance into a uniformly supercooled melt that is flowing around the crystal. It is well known that the dendrite tip speed and curvature are extremely sensitive to the variation of the surface energy along the crystal/melt interface and the anisotropy introduced by the crystalline structure. Only in the past few years have computational studies been reported of dendritic growth in the absence of flow that are fully validated against exact numerical

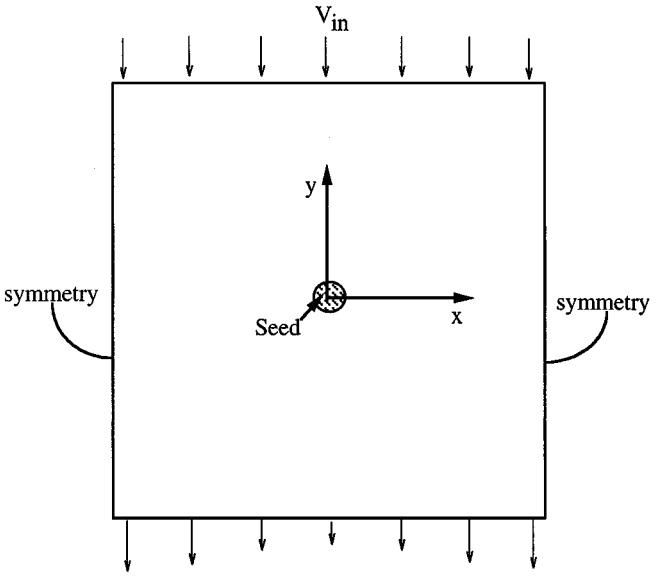

FIG. 11. Illustration of the physical system used in the simulation of free dendritic growth of a pure substance in a supercooled melt with and without melt convection.

solutions, such as microscopic solvability theory [14, 38–40]. Interestingly, most of these studies utilize the phase-field method. Although other computational methods have been employed to simulate dendritic growth in the absence of flow (e.g., Refs. [16, 17]), their results have not been fully validated. Here, we report on the first calculations of dendritic growth in the presence of convection. While we can compare our no-flow results to available benchmarks, no analytical solutions or computational results are available for comparison in the flow case. For the computations with convection, we present basic numerical tests that demonstrate the performance of the method for varying diffuse interface thickness and grid resolution.

The physical system is illustrated in Fig. 11. The domain size is square and a circular seed exists initially in the center. The crystal axes are aligned with the x-y coordinate axes. The melt flows from the top to the bottom with a uniform inlet velocity. Symmetry conditions are applied on the side walls of the domain. The initial velocities are taken to be those for steady flow around the seed. The inlet and initial melt temperature are the same. No noise was introduced into the calculations, preventing the growth of higher-order dendrite arms [38].

The phase-field equation employed in this example is the same as in Ref. [20] and takes the form in the present notation

$$g_s^2 \frac{\partial \phi}{\partial t} = \mu_k \Gamma \left[\nabla \cdot \left(g_s^2 \nabla \phi \right) - \frac{\partial}{\partial x} \left(g_s g_s' \frac{\partial \phi}{\partial y} \right) + \frac{\partial}{\partial y} \left(g_s g_s' \frac{\partial \phi}{\partial x} \right) - \frac{\phi(1-\phi)(1-2\phi)}{\delta^2} \right] + 5\mu_k (T_m - T) \frac{\phi^2 (1-\phi)^2}{\delta}, \tag{52}$$

where the term $g_s = 1 + \varepsilon_4 \cos 4\theta$ represents the anisotropy in the surface energy (for a crystal of cubic symmetry and anisotropy strength ε_4), $\theta = \arctan[(\partial\phi/\partial y)/(\partial\phi/\partial x)]$ is the angle between the interface normal and the crystal axis, and the prime denotes differentiation

with respect to θ. Aside from the inclusion of anisotropy, Eq. (52) is almost identical to Eq. (29). One difference is that the last term, $\phi(1-\phi)$ in Eq. (29), is replaced by $5\phi^2(1-\phi)^2$ in Eq. (52). The latter form corresponds to a greater concentration of the driving force at the center of the transition region ($\phi = 0.5$) and helps stabilize the front in the presence of a strong temperature gradient. (The multiplicative factor of 5 is a normalization introduced such that, with Γ and μ_k appearing explicitly in the phase-field equation, the standard interface condition is obtained in the limit $\delta \to 0$.) In the limit where δ is finite, the interface condition takes the form

$$\frac{V_n}{\mu_k^{eff}(\theta)} = T_m - T - \Gamma\left[g_s(\theta) + \frac{d^2 g_s(\theta)}{d\theta^2}\right]\kappa, \tag{53}$$

where

$$\frac{1}{\mu_k^{eff}(\theta)} = \frac{g_s(\theta)}{\mu_k}\left[1 - A\frac{\delta}{\alpha}\frac{\mu_k L}{c_p}\right] \tag{54}$$

and $A = 0.7833$. To carry out computations, it is useful to measure length and time in units of $W = \sqrt{2}\delta$ and $\tau = 2\delta^2/\mu_k\Gamma$, respectively, and to define the dimensionless temperature field $u = (T - T_m)/(L/c_p)$. In this case Eq. (52) can be written in the same form as in Ref. [20], where only the dimensionless coupling constant $\lambda = (5/4)(\delta/\Gamma)(L/c_p) = (5\sqrt{2}/8)(W/d_0)$ enters in the equation where $d_0 = \Gamma/(L/c_p)$ is the capillary length. Then, the term inside the square brackets on the RHS of Eq. (54) becomes equal to $1 - (4A/5)(\lambda W^2/\alpha\tau)$. In the present computations, we choose $D = \alpha\tau/W^2 = 4$ and choose accordingly $\lambda = 5/A = 6.383$, which makes $1/\mu_k^{eff}(\theta)$ vanish in Eq. (54), and yields the ratio $d_0/W = 0.139$. The other relevant parameters are $\varepsilon_4 = 0.05$ (5% anisotropy), and the Prandtl number, $Pr = 23.1$. In the simulations presented here the initial and inlet melt temperature is $u_{in} = -0.55$. Results are shown for inlet velocities $V_{in} = 0$ and 1, in units of W/τ.

The flow equations (9) and (10) are solved using the SIMPLER algorithm [35], while the phase-field equation and energy equation (12) are solved using an explicit method [38]. The species equation, Eq. (33), is not solved because we are simulating a pure substance. The time step is 0.008 in units of τ. Due to symmetry, only half of the domain ($x > 0$) is discretized using a square grid of 288×576 control volumes (unless otherwise noted). The spatial step is 0.4 in both the x and y directions in units of W. It is shown below that the present time and spatial steps lead to converged tip velocities and tip radii.

For diffusion controlled growth ($V_{in} = 0$), the present simulation recovers the results of Karma and Rappel [14]. As an example, Fig. 12 shows the phase-field contours and isotherms at three times corresponding to $t = 15$, 66, and 96 in units of τ. The dendrite grows symmetrically with the same dimensionless speed, equal to $V_{tip} = 0.502$ in units of W/τ, for all four tips. Rescaling the above tip velocity with $(\alpha\tau/W^2)/(d_0/W)$, it can be seen that the present value (0.01744) agrees well with the numerical solution (0.0174) and the Green's function analytical solution (0.017) reported in Refs. [14, 38]. More detailed comparisons and grid and convergence studies for diffusion controlled growth at other supercoolings and anisotropy strengths (using the same computer code for the phase-field equation) can be found in Refs. [14, 20, 38, 43]. We also performed a grid anisotropy test by rotating the principal growth direction of the dendrite by 45 degrees with respect to the grid. For the example corresponding to Fig. 12, the steady state tip velocity at 45 degrees was found to be 4.7% lower than the exact analytical value (0.017). A thorough analysis

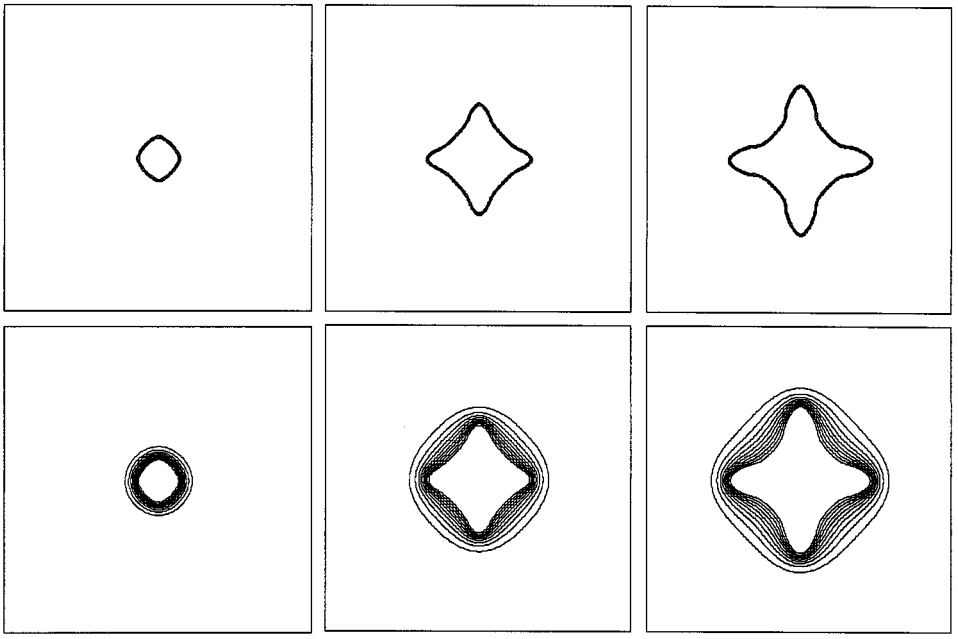

FIG. 12. Computed phase-field contours (top panels) and isotherms (bottom panels) from the dendritic growth simulation without convection at $t = 15$, 66, and 96 in units of τ (from left to right).

of the grid anisotropy effect in phase-field simulations of dendritic growth has recently been reported by one of the present authors [20]. According to that analysis, the present grid introduces an effective anisotropy that is only about 1% of the nominal interfacial anisotropy strength of 0.05.

Figure 13 shows the phase-field contours, velocity vectors, and isotherms for the simulation with convection ($V_{in} = 1$) at the same three times as Fig. 12. For better visualization, we have interpolated the velocities onto a grid that is almost 30 times coarser than the one used in the computations. The temperature field is significantly distorted and indicates much higher temperature gradients near the upper tip, where the flow impinges, than near the lower tip, in the wake of the dendrite. In fact, the isotherms and velocity vectors are not unlike the ones for low Reynolds number convection around an infinite cylinder. Consequently, the dendrite acquires a highly asymmetric shape, with the upper tip growing faster than the lower one. Another interesting observation is that the horizontal dendrite arms are no longer symmetric about the initial dendrite axis and appear to grow slightly upwards. This dendrite "tilting" is obviously not due to deformation of the solid (since it is assumed rigid), but due to the heat fluxes being higher on the upstream side than on the downstream side.

The evolution of all dendrite tip velocities, for two different grid resolutions, is plotted in Fig. 14a and compared to the pure diffusion case. The upper tip and the two horizontally growing tips experience a minimum in the velocity before approaching a steady value. The initial decrease and the minimum are caused by the melt temperature being initially uniform at $u_{in} = -0.55$. On the other hand, the lower tip does not approach a steady growth regime, which can be attributed to the fact that the convective flow in the wake region near the lower tip continues to weaken due to the ever increasing size of dendrite. It can be seen that the orientation of the dendrite tip with respect to the flow has a very strong effect on the

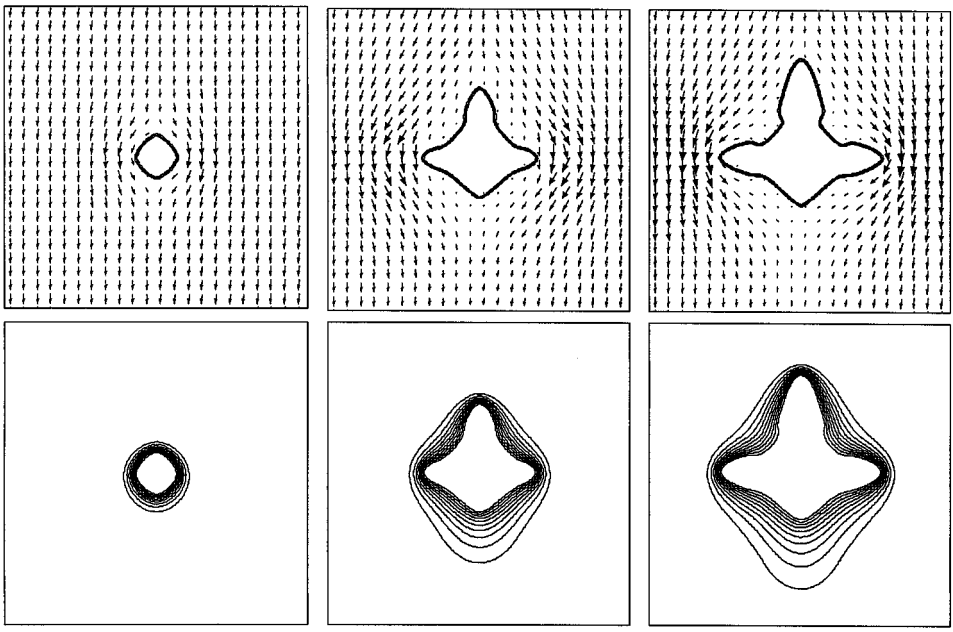

FIG. 13. Computed phase-field contours and velocity vectors (top panels) and isotherms (bottom panels) from the dendritic growth simulation with convection at $t = 15$, 66, and 96 in units of τ (from left to right).

steady tip velocities. The upper tip, where the flow impinges, grows about 40% faster than in the pure diffusion case, while the lower tip can be more than 30% slower. The horizontal tips, where the flow is normal to the growth direction, grow at approximately the same rate as in the diffusion case. These results are in qualitative agreement with the experimental data of Glicksman and Huang [41]. Although the present computational parameters do not correspond to the supercoolings investigated by Glicksman and Huang, and the flow in their experiments was induced by buoyancy, it can be estimated that the ratio of the flow velocity to the tip growth velocity for their measurements with $\Delta T = 0.515$ K was of the same order of magnitude as in the present simulation [i.e., O(1)]. Based on Fig. 27 in Ref. [2], convection in the $\Delta T = 0.515$ K experiments resulted in a roughly 40% enhancement in the velocity of the tip when the flow is opposite to the growth direction, and a reduction of around 60% for the tip growing parallel to the flow. Although this comparison is certainly not intended to be of a quantitative nature, and the actual percentages depend strongly on the flow velocity, it shows that the present computations give correct trends.

The results of some basic numerical tests of the present method for dendritic growth with convection are shown in Table II. In that table, computed steady state velocities (as well as tip radii; see below) of the upper tip that grows in a direction opposite to the flow are shown for varying grid resolution and diffuse interface thickness. It should be emphasized that the dendrite tip velocity is a good quantity to use in such tests, because it is easily measured from the computed results and, at the same time, highly sensitive to the tip operating state selection by the surface energy anisotropy. It can be seen that increasing the number of control volumes from 160×320 to 288×576 results in a roughly 10% decrease in the tip velocity. Doubling the resolution again from 288×576 to 576×1152 changes the tip velocity by only 1.6%, indicating that converged results are obtained with the 288×576 grid. A comparison of the evolution of all tip velocities for the two finer grids is shown in

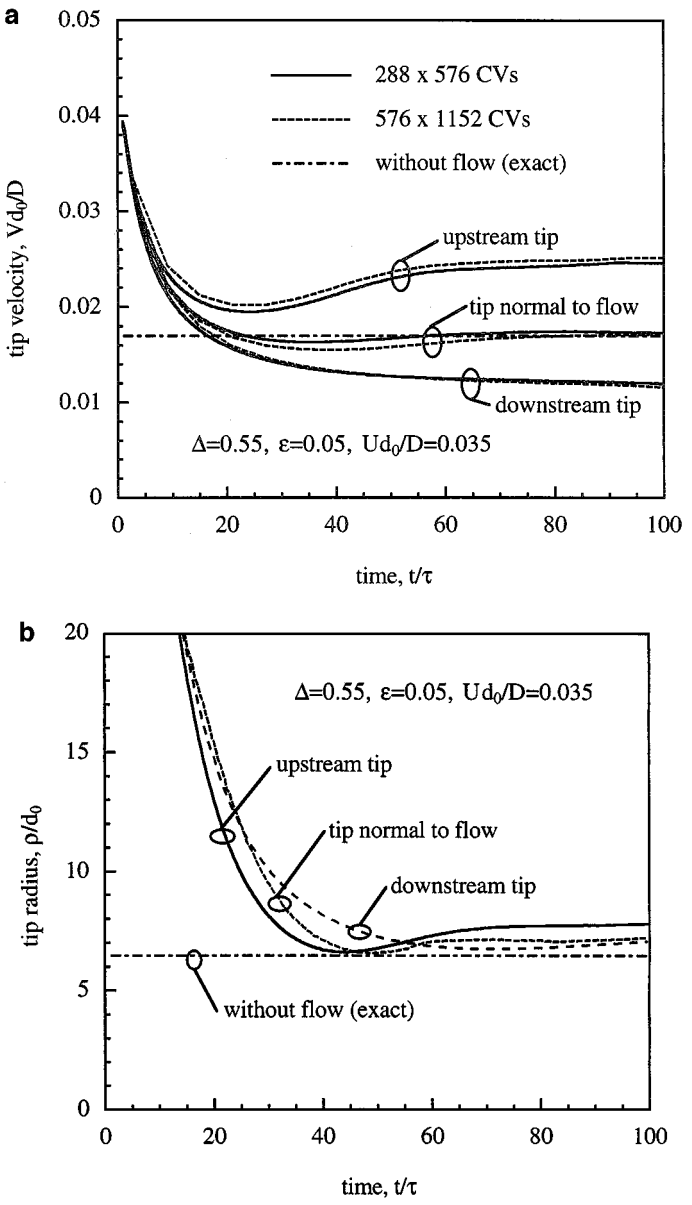

FIG. 14. Evolution of the tip velocities (a) and tip radii (b) measured from the results of the dendritic growth simulation.

Fig. 14a, and again consistent results are obtained. The diffuse interface thickness can be most easily varied by changing the diffusivity D; obviously for the phase-field method to be converged, the computed results should be independent of D and the interface thickness. In order to maintain the same number of control volumes over the thickness of the interface, the grid spacing must be adjusted accordingly. Table II shows that the upper tip velocities agree to within better than 2% for all three interface thicknesses tested. Although more detailed tests than shown in Table II should be conducted in the future, our results indicate that the present method with flow performs similar to phase-field methods without flow [14, 20, 38, 42]. Also noted in Table II are the CPU times used in the computations. These

TABLE II
Results of Grid Resolution and Diffuse Interface Thickness Tests for Phase-Field Simulations of Dendritic Growth with Convection

D	d_0/W	N_x	N_y	Vd_0/D	ρ/d_0	T_{CPU} [h]
4	0.139	160	320	0.0265	8.10	3
4	0.139	288	576	0.0240	7.51	8
4	0.139	576	1152	0.0244	7.46	31
3	0.185	320	640	0.0248	7.48	17
2	0.277	512	1024	0.0247	7.61	70

Note. Shown are the velocity, V, and radius, ρ, of the upper tip that grows in a direction opposite to the flow. In all tests the following parameters were held constant: $\Delta = 0.55$, $\varepsilon = 0.05$, $Pr = 23.1$, $Pe_\infty = Ud_0/D = 0.035$, $W = 1$, $\tau = 1$, $\Delta x/W = 0.4$. T_{CPU} denotes the CPU time in hours on a HP-C200 workstation; N_x and N_y are the number of control volumes in the x and y directions, respectively.

times should only be viewed as relative times as no effort was made to optimize the code. An almost linear relationship between the total number of control volumes and the CPU time can be noted. The CPU time increases with decreasing interface thickness, because smaller time steps must be used. The vast majority of the CPU time requirement is due to the flow solver, and more efficient numerical techniques can be used.

We have also measured the dendrite tip radii from the present simulation using a similar method as in Ref. [42]. The evolution of the radii ρ_{tip} is plotted in Fig. 14b. For all tips, the steady tip radii are only slightly above the pure diffusion value. For the upper tip, this can be attributed to two competing effects: the increased tip velocity due to flow would generally cause the tip radius to decrease because of stability considerations; however, the impinging flow also tends to make the heat fluxes along the interface more uniform, resulting in a tip shape that is more blunt. For the horizontal tip, the effect of the flow is minimal because the flow is normal to the growth direction. Despite the fact that the lower tip grows more slowly, the tip radius is about the same as in the diffusion case indicating that the flow in wake of the dendrite causes a more even distribution of the heat fluxes along the interface.

The knowledge of the tip radius and tip speed allows for the calculation of the tip Peclet number, defined as

$$Pe = \frac{V_{tip}\rho_{tip}}{2\alpha}. \tag{55}$$

For diffusion-controlled growth, the Peclet number is related to the dimensionless supercooling Δ at infinity by the two-dimensional Ivantsov relation [39]

$$\Delta = \sqrt{\pi Pe}\exp(Pe)\,\text{erfc}(\sqrt{Pe}). \tag{56}$$

For a supercooling of $0.55(= -u_{in})$, the Peclet number from the above equation is equal to $Pe^{IVAN} = 0.257$, while the Peclet number from the simulation with $V_{in} = 0$ is $Pe^{SIM} = 0.060$. The difference is in good agreement with the finding of Wheeler *et al*. [39] and Karma and Rappel [14, 38] that the ratio of Pe^{SIM}/Pe^{IVAN} decreases with increasing anisotropy. More discussion of this issue can be found in Refs. [20, 42].

Finally, we examine the tip selection criterion for convection influenced dendritic growth. Usually, the selection criterion is written as

$$\sigma^\star = [\rho_{tip}/d_0)Pe]^{-1}, \tag{57}$$

where $\sigma^\star$ is a stability or selection constant which varies with anisotropy strength (but is independent of supercooling) according to microscopic solvability theory [43, 44]. Based on the steady values of the tip radii and velocities in Figs. 14a and 14b, we find that $\sigma^\star = 1.48$ for the upper tip and $\sigma^\star = 2.42$ for the horizontal tips. For the lower tip, we estimate that $\sigma^\star = 3.4$ by averaging the tip velocity and radius from $t = 80$ to 100. For the pure diffusion case, we find that $\sigma^\star = 2.51$, which is in agreement with previous simulations and the Green's function analytical solution [14, 38]. The convection value of $\sigma^\star$ for the upper tip is significantly below the diffusion value. This finding may be compared to the solvability calculation of Bouissou and Pelcé [45] that predicts a variation of $\sigma^\star$ with the flow velocity. We are presently exploring this issue in more detail. The fact that the convection value of $\sigma^\star$ for the horizontal tips is quite close to the diffusion value is in agreement with the experiments of Bouissou *et al*. [46], who found that $\sigma^\star$ does not depend on the transverse component of the flow. The estimated $\sigma^\star$ for the lower tip is much higher than the diffusion value, indicating different growth mechanisms in the wake region. Obviously, this issue needs further investigation as well.

9. CONCLUSIONS

A diffuse interface or phase-field model is presented for the direct numerical simulation of microstructure evolution in solidification processes involving convection in the liquid phase. The mass, momentum, energy, and species conservation equations for the diffuse interface region are derived using volume averaging. An evolution equation for the phase field is obtained through a simplified geometrical derivation starting from the classical velocity-dependent Gibbs–Thomson equation for a sharp solid–liquid interface. The equations of the model are not derivable from a single Lyapovnov functional, but our computations demonstrate that this is not a limiting factor. In the limit of a thin interface, this model does indeed reduce to the classical equations and boundary conditions that one would write down for a macroscopically sharp interface, which makes this model computationally useful independently of the way in which it is derived. The phase-field equation, as well as the conservation equations, completely avoid the explicit tracking of the interface, the explicit satisfaction of interfacial conditions, and the calculation of interface normals and curvatures. Furthermore, it is possible to perform calculations in the limit of vanishing interface kinetic effects.

In accordance with the averaging method, the drag between the solid and liquid phases is modeled as a distributed momentum sink term in the diffuse interface region and is taken to be linearly proportional to the relative velocity of the phases. The interfacial drag model is calibrated for plane flow past a stationary solid–liquid interface and is shown to produce accurate results regardless of the diffuse interface thickness. The model is thoroughly tested against analytical results for two-dimensional Stokes flow through regular arrays of cylinders. These results indicate excellent convergence properties for large diffuse interface thickness to flow passage width ratios.

Two examples of application of the model to solidification/melting processes with melt convection are presented. The first example involves convection and coarsening in an isothermal mush of a binary alloy. Although the interface thickness is chosen to be unrealistically

large, the expected coarsening asymptotics are predicted. Results are presented for the evolution of the permeability of the mush due to coarsening. The second example represents the first fully resolved calculations of free dendritic growth of a pure substance in the presence of melt flow. The dendrite tip velocities, radii, and selection criterion in the presence of flow are examined in some detail. Additional simulations are needed to fully understand and characterize the system behavior in both of the above applications.

ACKNOWLEDGMENTS

This work was supported by the National Science Foundation (NSF) under Grant CTS-9501389 and NASA under contract NCC8-94. The research of A.K. was also supported by U.S. DOE Grant DE-FG02-92ER45471. We thank Dr. Qiao Li for his help in evaluating the tip radii and Dr. Houfa Shen for typing the manuscript.

REFERENCES

1. W. W. Mullins and R. F. Sekerka, Stability of a planar interface during solidification of a dilute binary alloy, *J. Appl. Phys*. **35**, 444 (1964).
2. Y.-W. Lee, R. N. Smith, M. E. Glicksman, and M. B. Koss, Effects of buoyancy on the growth of dendritic crystals, in *Annual Review of Heat Transfer*, edited by C. L. Tien (Begell House, New York, 1996), Vol. 7, p. 59.
3. M. Lifshitz and V. V. Slyozov, The kinetics of precipitation from supersaturated solid solutions, *J. Phys. Chem. Solids* **19**, 35 (1961).
4. C. Wagner, Theorie der Aeterung von Niederschlägen durch Umlösen (Ostwald-Reifung), *Z. Elektrochem*. **65**, 581 (1961).
5. R. Trivedi and W. Kurz, Dendritic growth, *Int. Mat. Rev*. **39**, 49 (1994).
6. S. R. Coriell, M. R. Cordes, W. J. Boettinger, and R. F. Sekerka, Effect of gravity on coupled convective and interfacial instabilities during directional solidification, *J. Cryst. Growth* **49**, 13 (1980).
7. S. H. Davis, Hydrodynamic interactions in directional solidification, *J. Fluid Mech*. **212**, 241 (1990).
8. R. Ananth and W. W. Gill, Dendritic growth of an elliptical paraboloid with forced convection in the melt, *J. Fluid Mech*. **208**, 575 (1989).
9. J. J. Xu, Dendritic growth from a melt in an external flow: Uniformly valid asymptotic solution for the steady state, *J. Fluid Mech*. **263**, 227 (1994).
10. H.-J. Diepers, C. Beckermann, and I. Steinbach, A phase-field method for alloy solidification with convection, in *Solidification Processing 1997*, edited by J. Beech and H. Jones (University of Sheffield, UK, 1997), p. 426.
11. G. Caginalp, Surface tension and supercooling in solidification theory, in *Applications of Field Theory to Statistical Mechanics*, edited by L. Garrido (Springer-Verlag, Berlin, 1985), p. 216.
12. A. A. Wheeler, W. J. Boettinger, and G. B. McFadden, Phase-field model for isothermal phase transitions in binary alloys, *Phys. Rev. A* **45**, 7424 (1992).
13. R. Kobayashi, Modeling and numerical simulations of dendritic crystal growth, *Phys. D* **63**, 410 (1993).
14. A. Karma and W.-J. Rappel, Phase-field method for computationally efficient modeling of solidification with arbitrary interface kinetics, *Phys. Rev. E* **53**, 3017 (1996).
15. H. S. Udaykumar and W. Shyy, Development of a grid-supported marked particle scheme for interface tracking, in *11th AIAA Comp. Fluid. Dyn. Conf*. (Orlando, FL, 1993), AIAA-93-3384.
16. D. Juric and G. Tryggvason, A front-tracking method for dendritic solidification, *J. Comput. Phys*. **123**, 127 (1996).
17. J. A. Sethian and J. Strain, Crystal growth and dendritic solidification, *J. Comput. Phys*. **98**, 231 (1992).
18. S. L. Wang *et al*., Thermodynamically-consistent phase-field models for solidification, *Phys. D* **69**, 189 (1993).
19. D. Jacqmin, An energy approach to the continuum surface tension method, in *34th AIAA Aerospace Sciences Meeting & Exhibit* (Reno, NV, 1996), AIAA-96-0858.

20. A. Karma and W.-J. Rappel, Quantitative phase-field modeling of dendritic growth in two and three dimensions, *Phys. Rev. E* **57**, 4323 (1998).
21. J. U. Brackbill, D. B. Kothe, and C. Zemach, A continuum method for modeling surface tension, *J. Comput. Phys*. **100**, 335 (1992).
22. M. Hassanizadeh and W. G. Gray, General conservation equations for multi-phase systems. I. Averaging procedure, *Adv. Water Resources* **2**, 131 (1979).
23. D. A. Drew, Mathematical modeling of two-phase flow, *Ann. Rev. Fluid Mech*. **15**, 261 (1983).
24. J. Ni and C. Beckermann, A volume-averaged two-phase model for transport phenomena during solidification, *Metall. Trans. B* **22**, 349 (1991).
25. D. J. Haymet and D. W. Octoby, A molecular theory for the solid-liquid interface, *J. Chem. Phys*. **74**, 2559 (1981).
26. J. Tiaden, B. Nestler, H. J. Diepers, and I. Steinbach, The multiphase-field model with an integrated concept for modelling solute diffusion, *Phys. D* **115**, 73 (1998).
27. A. Wheeler, W. J. Boettinger, and G. B. McFadden, Phase-field model of solute trapping during solidification, *Phys. Rev. E* **47**, 1893 (1993).
28. G. Caginalp and W. Xie, Phase-field and sharp-interface alloy models, *Phys. Rev. E* **48**, 1897 (1993).
29. J. W. Cahn and J. E. Hilliard, Free energy of nonuniform systems. I. Interface free energy, *J. Chem. Phys*. **28**, 258 (1958).
30. L. D. Landau and E.M. Lifshitz, *Statistical Physics* (Pergamon, New York, 1980).
31. A. Karma, unpublished notes.
32. E. Brener and V. I. Melnikov, Velocity selection and instability spectrum in 3D dendritic growth, *J. Exp. Theoret. Phys*. **80**, 341 (1995).
33. A. S. Sangani and A. Acrivos, Slow flow through a periodic array of spheres, *Int. J. Multiphase Flow* **8**, 343 (1982).
34. J. E. Drummond and M. I. Tahir, Laminar viscous flow through regular arrays of parallel solid cylinders, *Int. J. Multiphase Flow* **10**, 515 (1984).
35. S. V. Patankar, *Numerical Heat Transfer and Fluid Flow* (Hemisphere, Washington, DC, 1980).
36. J. A. Marqusee, Dynamics of late stage phase separations in two dimensions, *J. Chem. Phys.* **81**, 976 (1984).
37. L. Ratke and W. K. Thieringer, The influence of particle motion on ostwald ripening in liquids, *Acta Metall*. **33**, 1793 (1985).
38. A. Karma and W.-J. Rappel, Phase-field modeling of crystal growth: New asymptotics and computational limits, in *Mathematics of Microstructural Evolution*, edited by L.-Q. Chen *et al*. (TMS and SIAM, Warrendale, PA, 1996), p. 204.
39. A. A. Wheeler, B. T. Murray, and R. J. Schaefer, Computation of dendrites using a phase field model, *Phys. D* **66**, 243 (1993).
40. T. Ihle and H. Muller-Krumbhaar, Fractal and compact growth morphologies in phase transitions with diffusive transport, *Phys. Rev. E* **49**, 2972 (1994).
41. M. E. Glicksman and S. C. Huang, Convective heat transfer during dendritic growth, in *Convective Transport and Instability Phenomena*, edited by J. Zierip and H. Oertel, Jr. (G. Braun, Karlsruhe, West Germany, 1982), p. 557.
42. A. Karma and W.-J. Rappel, Numerical simulation of three-dimensional dendritic growth, *Phys. Rev. Lett*. **77**, 4050 (1996).
43. J. S. Langer, Existence of needle crystals in local models of solidification, *Phys. Rev. A* **33**, 435 (1986).
44. P. Pelcé, *Dynamics of Curved Fronts* (Academic Press, New York, 1988).
45. P. Bouissou and P. Pelcé, Effect of forced flow on dendritic growth, *Phys. Rev. A* **40**, 6673 (1989).
46. P. Bouissou, B. Perrin, and P. Tabeling, Influence of an external flow on dendritic crystal growth, *Phys. Rev. A* **40**, 509 (1989).